SPH MODELING OF VORTICITY GENERATION BY SHORT-CRESTED WAVE BREAKING

Zhangping Wei[1], Robert A. Dalrymple[2]

This study investigates vorticity generation by short-crested wave breaking by using the mesh-free Smoothed Particle Hydrodynamics model, GPUSPH. The short-crested waves are created by generating intersecting wave trains in a numerical wave basin with a beach. The capability of GPUSPH to simulate short-crested waves is first validated by laboratory measurements. Then we examine short-crested wave breaking with two incident wave heights $H = 0.2$ m and 0.3 m. The larger incident wave breaks at the toe of the planar beach, while the smaller incident wave breaks above the planar beach. The breaking wave profile, current field, nearshore circulation pattern, and vertical vorticity field due to short-crested wave breaking are carefully compared between two incident waves.

Keywords: GPUSPH; Short-crested waves; Wave breaking; Nearshore circulation; Vertical vorticity, Vortex

INTRODUCTION

Nearshore breaking waves are often short-crested due to random sea states and directional spread of waves. Peregrine (1998) suggested that short-crested wave breaking generates vertical vorticity, which describes the horizontal rotation of flows. By use of the open-source Smoothed Particle Hydrodynamics (SPH) model GPUSPH (Hérault et al., 2010), we recently conducted numerical experiments to investigate short-crested waves in the surf zone (Wei et al., 2017). Due to the relatively strong nonlinearity, the generated short-created waves breaking at the toe of the planar beach, and we observed rip currents as discussed in Dalrymple (1975) and undertow created by synchronous intersecting waves. We also found that the superposition of intersecting waves and the interaction between rip current and the crest end of short-crested waves create smaller isolated breakers in the outer surf zone. Furthermore, the non-uniformity of wave breaking alongshore causes wave-wave interaction and wave amplitude diffraction that induce alongshore wave number variation. We also observed the existence of 3D vortices and multiple circulation cells with a rotation frequency much lower than the incident wave frequency across the outer surf zone to the beach. By following the Kelvin's circulation theorem, we were able to measure the vertical vorticity generated by short-crested wave breaking with a limited number of wave components, and also under a directional wave spectra. Although the observations in Wei et al. (2017) are significant and interesting, we did not verify our findings by considering a different incident wave height. This motivates us to re-examine the numerical experiment in Wei et al. (2017) by using a smaller wave height in this work.

The rest of the paper is organized as follows. We first briefly review the generation of short-crested waves by using the synchronous wave trains method of Dalrymple (1975). Then we validate the capability of GPUSPH to simulate short-crested waves propagation by using laboratory data. Next we examine the wave field, hydrodynamic field, and vorticity generation by short-crested wave breaking over a planar beach with a different wave height as used in Wei et al. (2017). Finally we summarize the findings of this work.

THE SYNCHRONOUS WAVE TRAINS METHOD

This study generates short-crested waves by following Dalrymple (1975) by superimposing intersecting wave trains of the same wave period. The detailed derivation for wave generation has been given by Wei et al. (2017), and we review it briefly in this section for the completeness of this work. Given a coordinate system (x, y, z), where position x axis is the onshore direction, and y axis is the alongshore direction, we assume that two wave trains of the same period T with the same amplitude propagate to the shore from two different directions, such that the wave rays make angles α and β clockwise from the positive x axis. The free surface profile at the offshore boundary (i.e., $x = 0$) where the intersecting wave trains are generated by a series of wavemakers is

$$\eta(0, y, t) = \frac{H}{2} \cos\left[\frac{k}{2}(\sin\alpha_w + \sin\beta_w)y + \sigma t\right] \cos\left[\frac{k}{2}(\sin\alpha_w - \sin\beta_w)y\right] \tag{1}$$

where t is the time; k is the wave number $(2\pi/L)$; σ is the angular frequency of the waves $(2\pi/T)$; and H is the initial wave height of the intersecting wave trains; the subscript w indicates information at wavemakers.

[1]Department of Civil Engineering, Johns Hopkins University, Baltimore, MD 21218, USA (corresponding author). E-mail: zwei@jhu.edu; zwei.coast@gmail.com

[2]Department of Civil Engineering, Johns Hopkins University, Baltimore, MD 21218, USA. E-mail: rad@jhu.edu

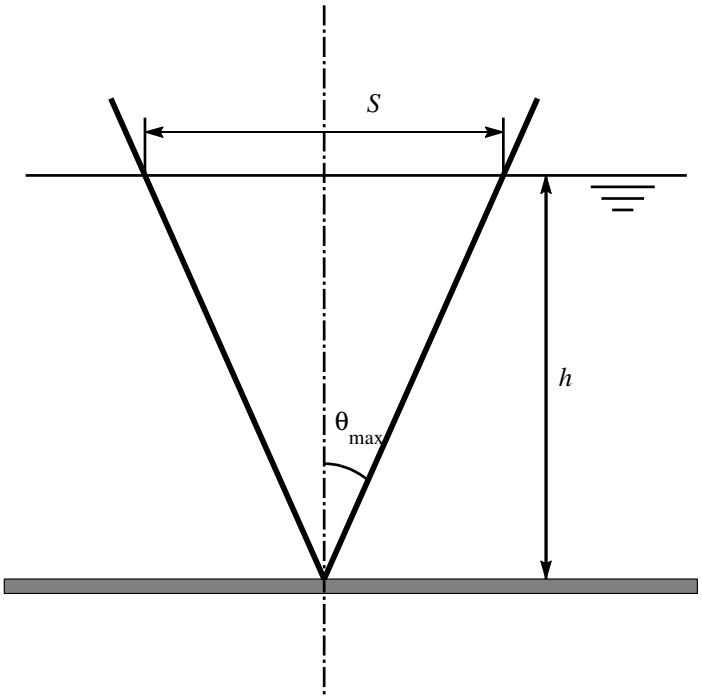

Figure 1: Definition sketch of a flap-type wavemaker (Wei et al. (2017)).

Considering a flap-type wavemaker as shown in Figure 1, the maximum rotation angle is defined by

$$\theta_{max} = \tan^{-1}\left(\frac{S/2}{h}\right) \tag{2}$$

where h is the local water depth at the flap-type wavemaker, and the stroke S is given by Dean and Dalrymple (1991) as

$$\frac{H}{S} = 4\left(\frac{\sinh kh}{kh}\right)\frac{kh\sinh kh - \cosh kh + 1}{\sinh 2kh + 2kh} \tag{3}$$

By taking into account the alongshore variation of free surface profile as indicated in Eq. (1), we obtain the instantaneous rotation angle for all wavemakers along the offshore boundary as

$$\theta(0, y, t) = \theta_{max}\sin\left[\frac{k}{2}(\sin\alpha_w + \sin\beta_w)y + \sigma t\right]\cos\left(\frac{\pi}{\lambda}y\right) \tag{4}$$

where the spacing between rip currents or the distance between two nodal (or antinodal) lines is given as

$$\lambda = \frac{L}{\sin\alpha_w - \sin\beta_w} \tag{5}$$

Dalrymple (1975) also pointed out that there is an angular deviation between the nodal lines and the x axis if the two incident angles are not equal but opposite. The angular deviation is written as

$$\varphi = \tan^{-1}\left(\frac{\cos\beta_w - \cos\alpha_w}{\sin\alpha_w - \sin\beta_w}\right) \tag{6}$$

The dimension of the considered wave basin is (l_x, l_y, l_z). It consists of b_x long offshore flat and a planar beach with slope equal to m. In terms of the numerical boundary condition, at the offshore boundary the intersecting waves are generated by a series of flap-type wavemakers. For the shoreward boundary, a

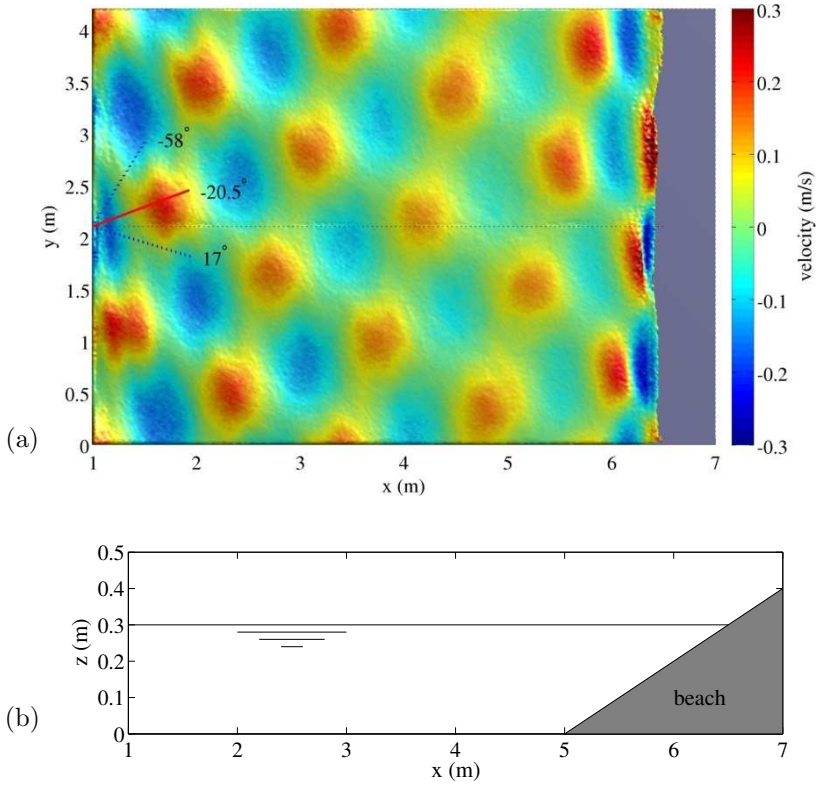

Figure 2: Numerical validation of the two wave trains experiment of Dalrymple (1975) (α_w = 17°, β_w = -58°, and φ = -20.5° from Eq. (6)). (a) Top view of the wave field, and the colorbar shows the cross-shore velocity, and (b) side view of the bed profile.

planar beach is used to attenuate the incoming waves. Regarding the numerical discretization in GPUSPH, the whole basin is discretized into a set of particles with a particle size Δp, and a set of moving boundary particles that represent the offshore wavemakers are driven by Eq. (4).

MODEL VALIDATION

Wei et al. (2017) validated the capability of GPUSPH to generate short-crested waves by using a large-scale laboratory experiment, this study further validates the model by considering an experiment with oblique short-crested waves near the beach. In addition to the derivation of short-crested waves generation method as presented in the previous section, Dalrymple (1975) also conducted a laboratory experiment to verify the derived rip current spacing. The laboratory basin consisted of a flat offshore bottom and a planar beach with an approximate slope of m = 1:5. The water depth was about h = 0.3 m near the wavemaker. Due to the equipment constraints, the intersecting wave trains of the same wave period T = 0.903 s, and the same wave height H = 0.055 m were generated by reflecting the incident wave from an offshore vertical wall, oriented at an angle with respect to the shoreline. The resulting incident wave angles were $\alpha_w = 17°$ and $\beta_w = -58°$ with respect to the normal direction of the beach. Since the two incident wave angles are not symmetric, the generated short-crested waves propagate toward the beach with an angle determined by Eq. (6), which gives $\varphi = -20.5°$.

In GPUSPH, the horizontal offshore flat is about b_x = 5 m, and the wavemakers are placed offshore at x = 1 m. Instead of generating the incident waves by the reflecting wall method used in the laboratory, waves in the numerical simulation are generated by the method presented in the previous section. To address the oblique incidence in the laboratory, a numerical periodic boundary condition is achieved at the alongshore boundaries by two steps. First, we estimate initial basin widths l_{y1} and l_{y2} by enforcing the periodicity for the *sine* and *cosine* terms respectively in Eq (4) by

$$\frac{k}{2}(\sin\alpha_w + \sin\beta_w)\cdot l_{y1} = 2n_1\pi, \qquad (n_1 = 1, 2, 3, \cdots) \tag{7a}$$

$$\frac{\pi}{\lambda} l_{y2} = 2n_2\pi, \qquad (n_2 = 1, 2, 3, \cdots) \tag{7b}$$

Then we determine the basin width l_y by

$$l_y = n_1 l_{y1} = n_2 l_{y2} \tag{8}$$

In this way, we will always have $\eta(x, y = 0, t) = \eta(x, y = l_y, t)$ and $\theta(x, y = 0, t) = \theta(x, y = l_y, t)$, resulting in a perfect periodic boundary in the alongshore direction.

The alongshore basin width is determined by Eqs. (7) and (8), and it is about 4.2 m. Regarding the numerical discretization, the numerical wave basin is discretized into particles, with a particle size of Δp = 0.01 m. resulting in 30 particles over the water column offshore and a total number of 6.1 million particles. Among them, there are about 5.8 million fluid particles, and the rest amount of particles are used to represent the flap-type wavemakers and the wave basin.

The numerical simulation of the experiment of Dalrymple (1975) is shown in Figure 2. Figure 2(a) shows the overhead view of free surface profile, and Figure 2(b) shows the sideview of the wave basin. The free surface profile is detected by a method presented by Wei et al. (2016), and the method is able to resolve realistic 3D breaking waves due to wave-structure interaction (Wei et al. (2015), Wei and Dalrymple (2016)). First, the theoretical angular deviation determined by Eq. (6) is about $-20.5°$. Figure 2(a) shows that the nodal line of short-crested waves is about $\varphi = -20.5°$ with respect to the x axis. Furthermore, the theoretical rip spacing is about 1.05 m, one would expect that there are about four nodal lines in the numerical basin, which are also clearly shown by the numerical model. Last but not least, the honeycomb shape of short-crested waves in Figure 2(a) is very similar to the wave profile observed by Hammack et al. (1989) in the laboratory. Overall, this numerical test case further validates that GPUSPH is able to accurately generate short-crested waves based on the method of Dalrymple (1975).

SHORT-CRESTED WAVE BREAKING OVER A PLANAR BEACH

We follow Wei et al. (2017) to set up our numerical wave basin. The wave basin is made of an offshore horizontal flat of b_x = 4 m and a planar beach with a mild slope of m = 1:50. A series of flap-type wavemakers are located along the y axis at x = 1 m, and the offshore water depth is set to be h = 0.5 m. We consider two incident wave trains with the same wave period of T = 2 s. The two incident wave angles are equal but opposite ($\alpha_w = -\beta_w = 11.71°$). By using Eq. (5), we obtain the nodal line spacing λ = 10 m. Then the alongshore basin width is chosen to be $l_y = 2\,\lambda$ = 20 m, and two shore-normal nodal lines are formed at y = 5 and 15 m alongshore. Different from the wave height of H = 0.3 m used by Wei et al. (2017), we consider a smaller wave with H = 0.2 m. In GPUSPH, the full basin is discretized into particles, with a fixed particle size of Δp = 0.02 m, resulting in 25 particles over the water column offshore and a total number of 18.5 million particles for the whole basin. At the two alongshore boundaries at the antinodal lines, the no-flow wall boundary condition is applied. In the following sections, we will compare the breaking wave profile, current field, nearshore circulation pattern, and vertical vorticity field associated with short-crested waves generated by an incident wave height H = 0.2 m to those associated with short-crested waves generated by H = 0.3 m, as reported in Wei et al. (2017).

Breaking wave profile

Figure 3(a) and (b) show the instantaneous wave field colored by the elevation up to x = 25 m nearshore for both wave heights H = 0.2 m and 0.3 m, respectively. For the case with H = 0.2 m in Figure 3(a), waves are subject to shoaling once they propagate over the planar beach starting at x = 4 m, resulting in a curvy wave crest. Eventually they break around x = 15 m and then propagate nearshore as bores. For the case with H = 0.3 m in Figure 3(b), the short-crested waves break over the planar beach starting at x = 4 m shortly after they are generated at x = 1 m by the wavemakers. Wave breaking is initiated at the center of the short crest, spreading alongshore in both directions, towards the nodal lines. A series of isolated waves (i.e., individual waves with a higher wave height) are then generated at the crest ends. The generation of isolated waves is attributed to two factors as explained by Wei et al. (2017). The major factor is the superposition of the two crest ends of intersecting waves (e.g., around x = 5 m and y = 6 m), resulting in an increase of

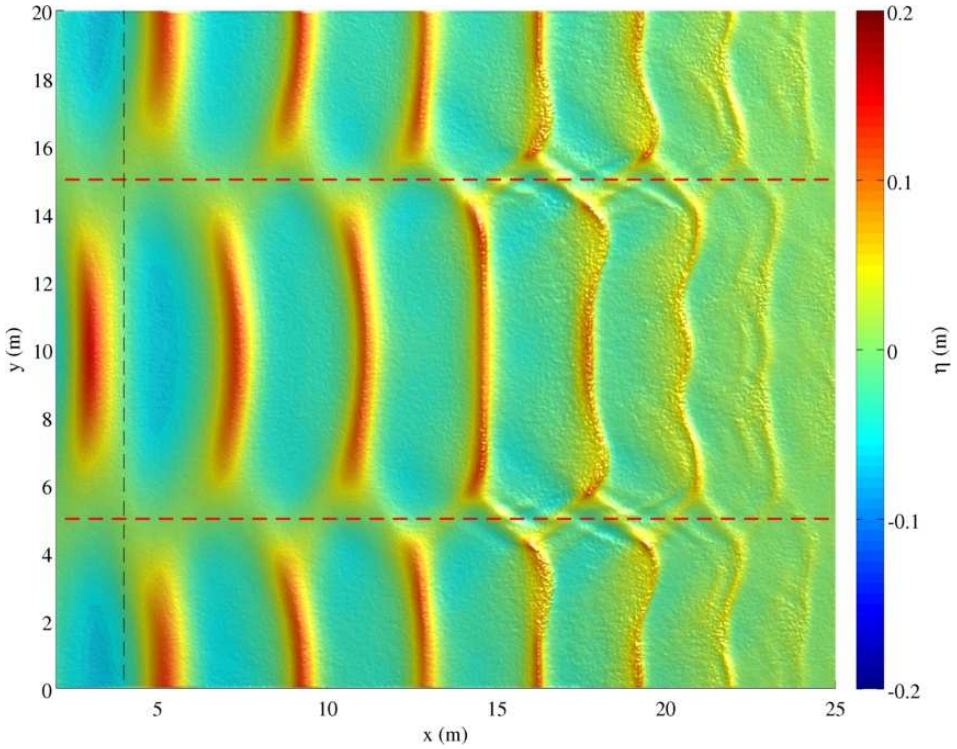

(a) H = 0.2 m

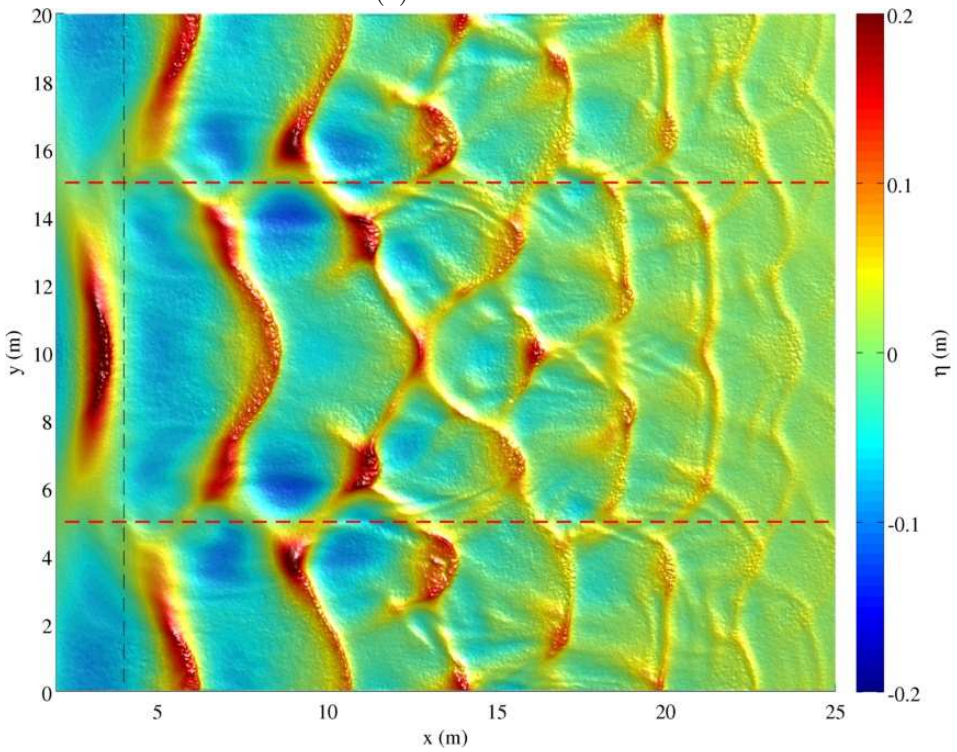

(b) H = 0.3 m

Figure 3: Top view of short-crested wave field at t = 80 s. (a) H = 0.2 m, and (b) H = 0.3 m (Wei et al. (2017)). The dashed line at x = 4 m indicates the starting point of the beach, and the red dashed lines indicate the nodal lines at y = 5 and 15 m.

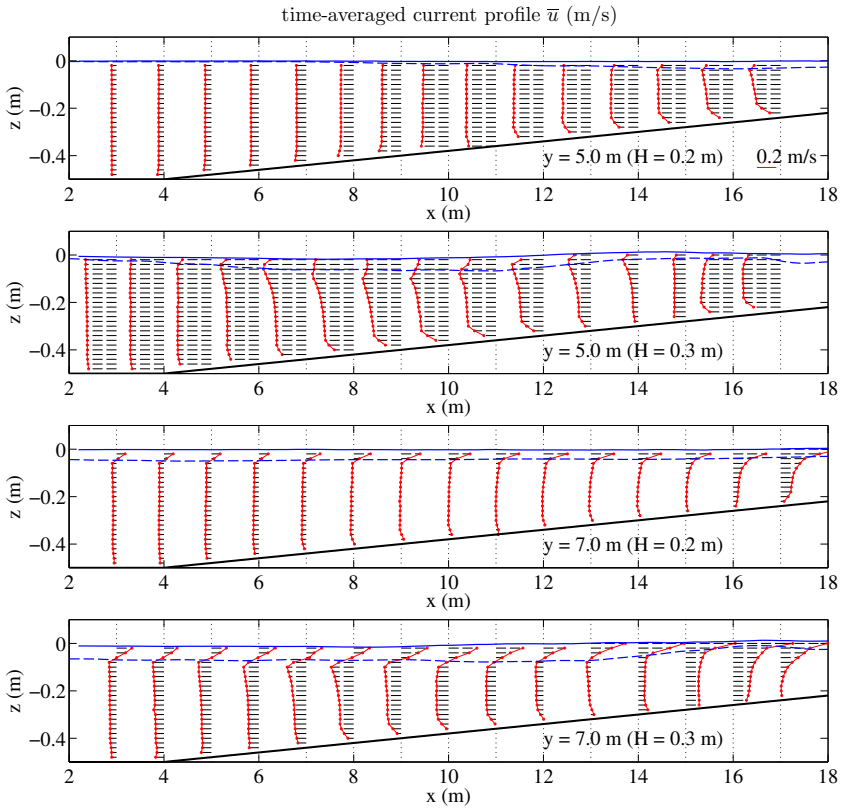

Figure 4: The vertical profile of the time-averaged cross-shore velocity at two sections (y = 5 and 7 m) for H = 0.2 m and H = 0.3 m (Wei et al. (2017)), and each section has 15 locations (x = 3 to 17 m). The zero velocity is set at the individual cross-shore location (e.g., x = 10 m); the plot is at its right side if the velocity is positive, otherwise the plot is at its left side. The blue solid line indicates the mean water level; the blue dashed line indicates the wave trough; and the vertical resolution is one particle size of Δp = 0.02 m.

local wave height at that location. A secondary factor, which takes place only after the development of rip currents, is wave-current interaction. Basically the rip current near y = 5 m opposes and further slows down the onshore propagation of the crest end, resulting in local wave amplification and separation of isolated waves from the head of short-crested waves. Figure 3 (b) also shows that there are a large number of small waves (both in wave height and wave length) observed starting around x = 15 m nearshore. That is due to the interaction among the isolated waves, resulting in nodal line bifurcation.

Current field & nearshore circulation

The time-averaged velocity at any point is defined by

$$\overline{\vec{u}(x,y,z)} = \frac{1}{n_w T}\int_{t_0}^{t_0+n_w T} \vec{u}(x,y,z,t)\mathrm{d}t \tag{9}$$

where $t_0 = 40T$ is the start time of the measurement, the total number of waves sampled is $n_w = 10$, the SPH particle averaged velocity $\vec{u}$ has three components (u, v, w). Figure 4 shows numerical predictions of the vertical distribution of the time-averaged cross-shore velocity $\overline{u(x,y,z)}$ for both H = 0.2 m and 0.3 m. For each case, there are two alongshore sections (y = 5 and 7 m), with each section has 15 locations (x = 3 to 17 m) from offshore to nearshore. The section along y = 5 m is at a nodal line where the rip current is formed, as demonstrated by the negative current along this line. It is also seen that the vertical profile of current is relatively uniform over the water column. For the case with H = 0.2 m, the wave breaks over the upper part of the beach, as a result, the rip current is confined in a region above the beach slope. For the case with H = 0.3 m, the wave breaks near the toe of the beach, and the resulting rip current is observed offshore. The section along y = 7 m is between the breaking wave crest end and the crest head, and the

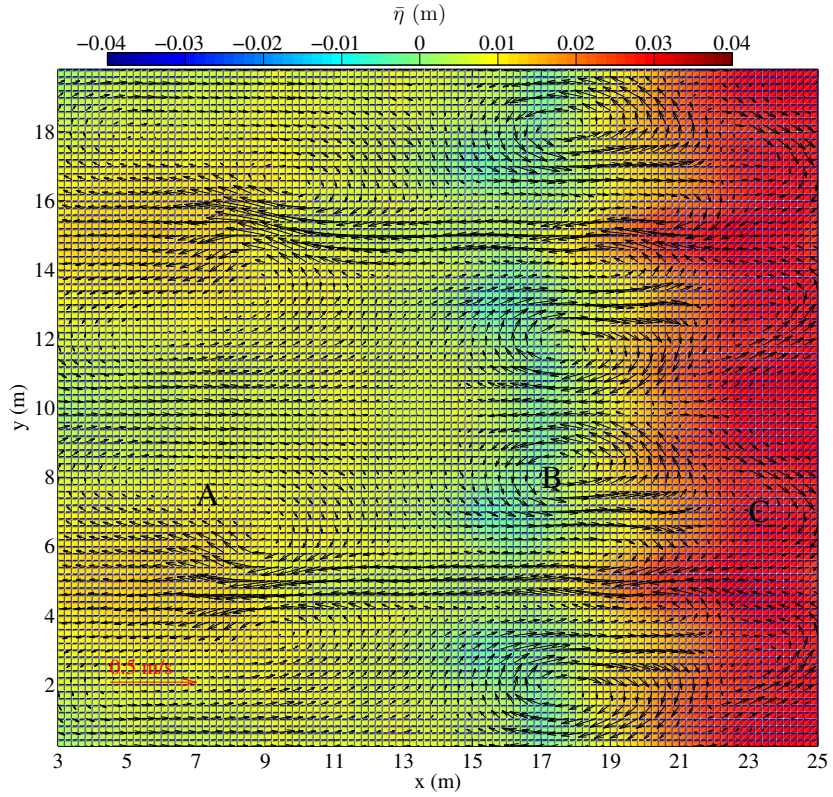

(a) H = 0.2 m

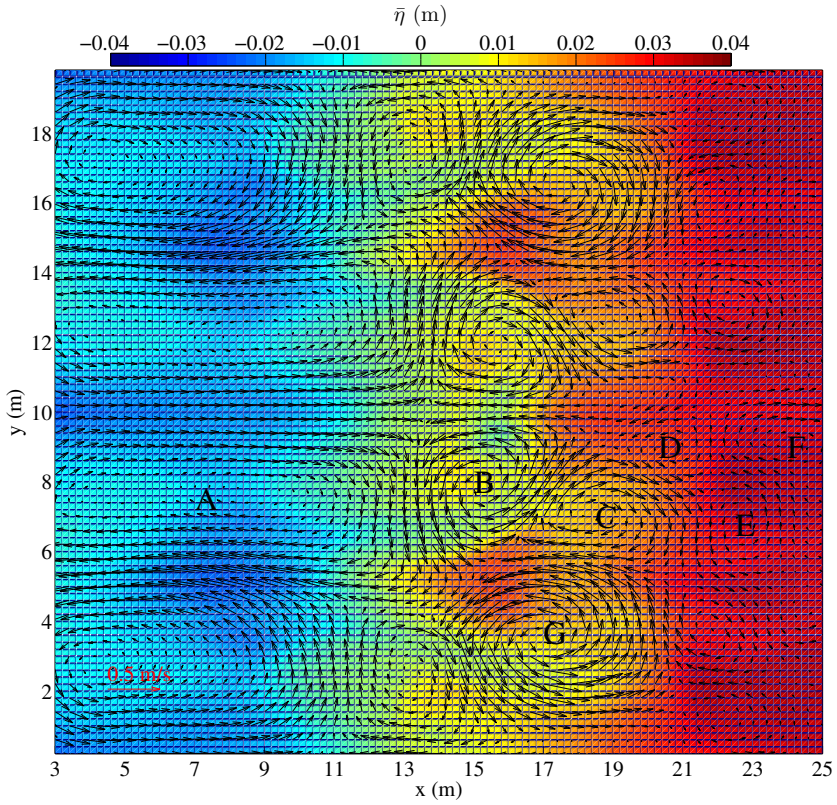

(b) H = 0.3 m

Figure 5: The distribution of the mean water level overlain by the time- and depth-averaged current field over 10 wave periods ($40T - 50T$). (a) H = 0.2 m, and (b) H = 0.3 m (Wei et al. (2017)). The alphabet letters indicate the circulation cells cross the wave basin. Different vector scales are used in the two plots.

numerical model shows the existence of undertow (a steady, offshore-directed current that compensates for the mass transport by breaking waves) for the case with $H = 0.3$ m. However, the current profile at section $y = 7$ m is very weak for the case with $H = 0.2$ m.

Next we analyze the mean water level and the current field over the basin. The mean water level is obtained by

$$\overline{\eta(x,y)} = \frac{1}{n_w T}\int_{t_0}^{t_0+n_w T} \eta(x,y)\mathrm{d}t \tag{10}$$

and the time- and depth-averaged velocity is defined by

$$\overline{\langle \vec{u}(x,y)\rangle} = \frac{1}{z_0 - z_b}\frac{1}{n_w T}\int_{z_b}^{z_0}\int_{t_0}^{t_0+n_w T} \vec{u}(x,y,z,t)\mathrm{d}z\mathrm{d}t \tag{11}$$

where z_b is the bottom of the basin, and z_0 is the mean water level. Figure 5 shows the distribution of mean water level overlain by the current field for both $H = 0.2$ m and 0.3 m. Due to the fact that the short-crested waves break mainly above the beach with $H = 0.2$ m, the rip current shown in Figure 5(a) does not go offshore as far as the one in Figure 5(b), and the rip current pattern in Figure 5(a) is similar to the distribution observed by Hammack et al. (1991) in the laboratory. The current field in Figure 5 also indicates the existence of basin circulation in both cases, but there are still some differences regarding the circulation pattern. First of all, the short-crested wave breaking with $H = 0.3$ m drives much stronger nearshore circulation than the one with $H = 0.2$ m (Note that different vector scales are used in Figure 5(a) and (b)). Secondly, there are different number of cells observed in Figure 5(a) and (b). The case with $H = 0.2$ m has about three circulation cells formed from the outer surf zone to the beach, but there are five circulation cells with $H = 0.3$ m. Wei et al. (2017) pointed out that in Figure 5(b) there are several vortices associated with circulation cells, e.g., B and G, as the current flows around the vortex core that has a lower mean water level. The existence of vortices explains the unusual phenomenon: currents flow against the wave setup in, e.g., cells B and G. It is likely that there is also a vortex at the circulation cell B in Figure 5(a), where the circulation current also flows against the wave setup.

The vertical vorticity that describes the horizontal rotation of the flows is defined by

$$\omega_z = \frac{\partial u_y}{\partial x} - \frac{\partial u_x}{\partial y} \tag{12}$$

Furthermore, the time-averaged vertical vorticity and the time- and depth-averaged vertical vorticity can be computed by Eqs. (9) and (11) with Eq. (12) as the input, respectively. Figure 6 shows the top view of instantaneous vertical vorticity field on the free surface under short-crested wave breaking for both $H = 0.2$ m and 0.3 m. The vorticity is computed based on the definition of Eq. (12), and the vorticity field is antisymmetric with respect to the centerline at $y = 10$ m for both wave heights. Figure 6(a) shows that the distribution of the vertical vorticity mainly follows the breaking wave crests, and the vertical vorticity in the rest of wave basin is very small. This confirms that the generation of vertical vorticity is attributed to short-crested wave breaking. Wei et al. (2017) showed that there is a vertical variation of vertical vorticity over the water column in the diffracted wave zone (e.g., $x > 15$ m) for $H = 0.3$ m in Figure 6(b), corresponding to a vertical variation of horizontal flow rotation (or a 3D turbulent flow field).

Figure 7 shows the time- and depth-averaged current field and the associated time- and depth-averaged vertical vorticity field from outer surf zone ($x = 3$ m) to the beach ($x = 25$ m) for both $H = 0.2$ m and 0.3 m (Note that different vector and color scales are used in Figure 7(a) and (b)). It is seen that the flow rotation direction is consistent with the sign of the vertical vorticity field (i.e., a positive vertical vorticity corresponding to an anti-clockwise circulation cell, and a negative vertical vorticity corresponding to a clockwise circulation cell). Wei et al. (2017) showed that at circulation cells B, C, and G (the locations of vortices) in Figure 7(b), there are relatively large mean vertical vorticity. As a result, the strong vortex motion drives the current pattern at circulation cell G, and also current against wave setup at circulation cells B and C, as seen in Figure 5(b). For the case with $H = 0.2$ m, short-crested waves break over the planar beach starting at $x = 15$ m, wave breaking also drives the formation of vortex structure, e.g., cell B in Figure 7(a). It is seen that there are opposite signed vertical vorticity regions cross the two nodal lines $y = 5$ and 15 m, where the rip currents are formed. Our observation confirms the work of Johnson and Pattiaratchi (2006) that rip currents are generated in a region with opposite signed vertical vorticity.

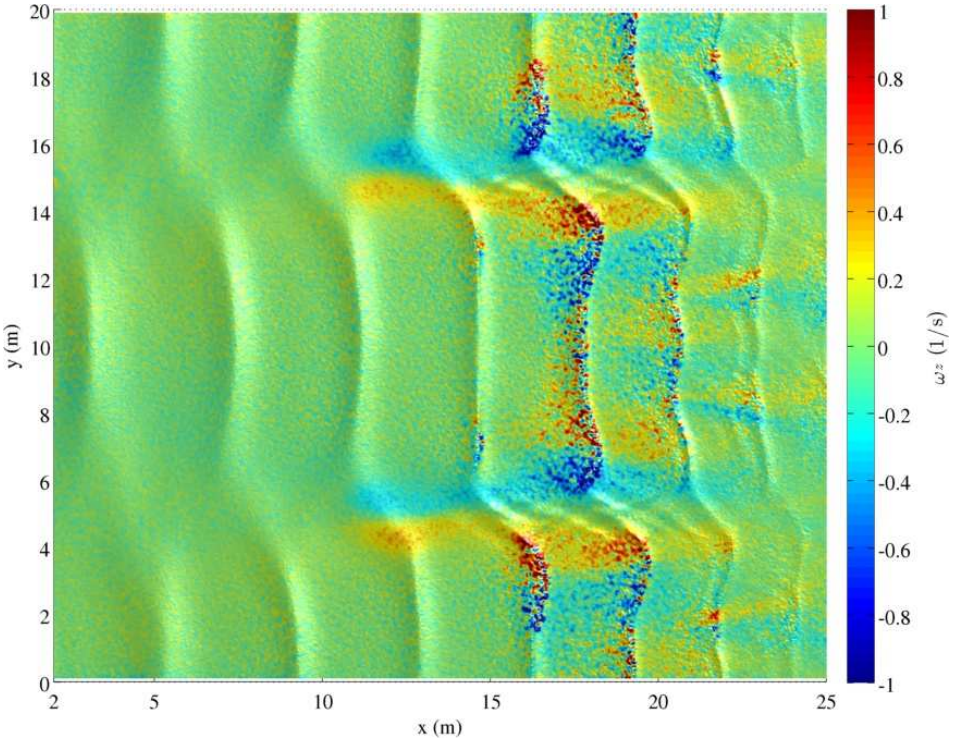

(a) H = 0.2 m

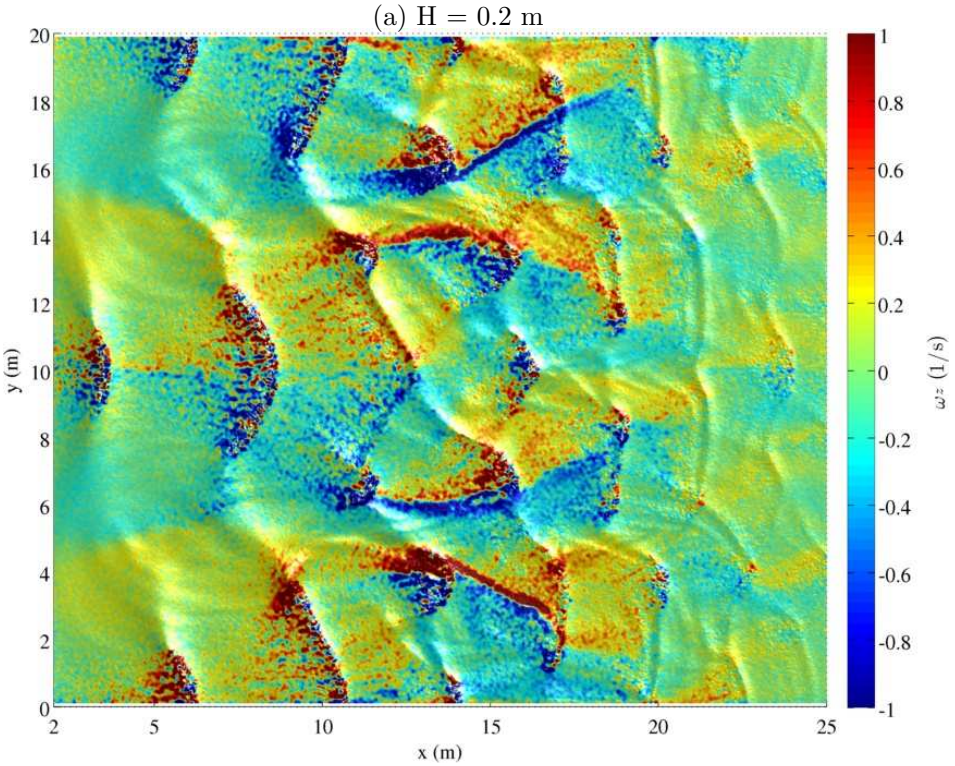

(b) H = 0.3 m

Figure 6: Top view of the vertical vorticity under short-crested wave breaking at t = 80 s. (a) H = 0.2 m, and (b) H = 0.3 m (Wei et al. (2017)).

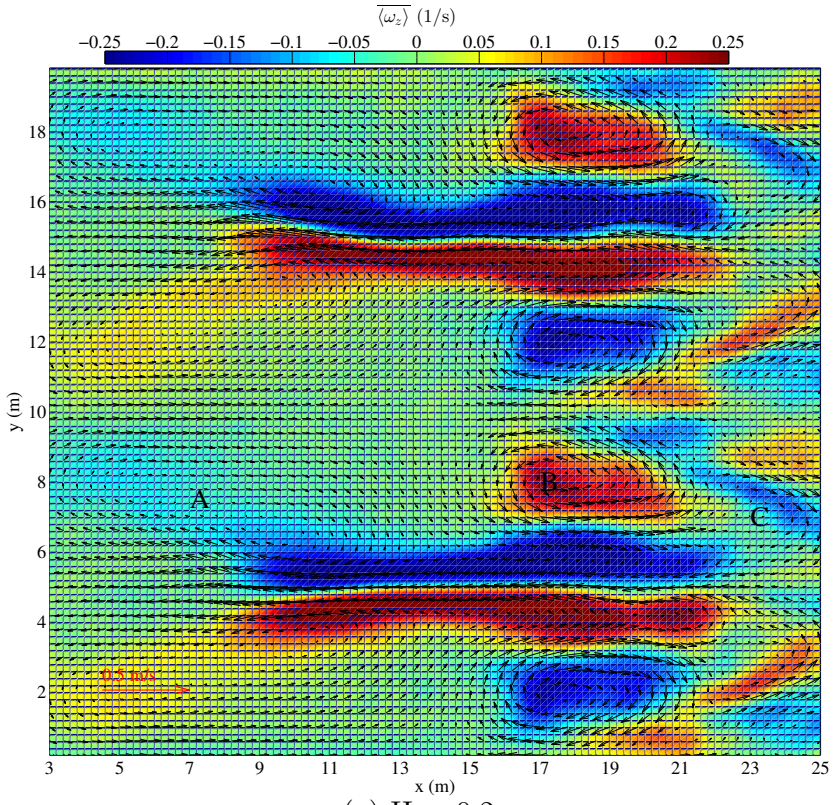

(a) H = 0.2 m

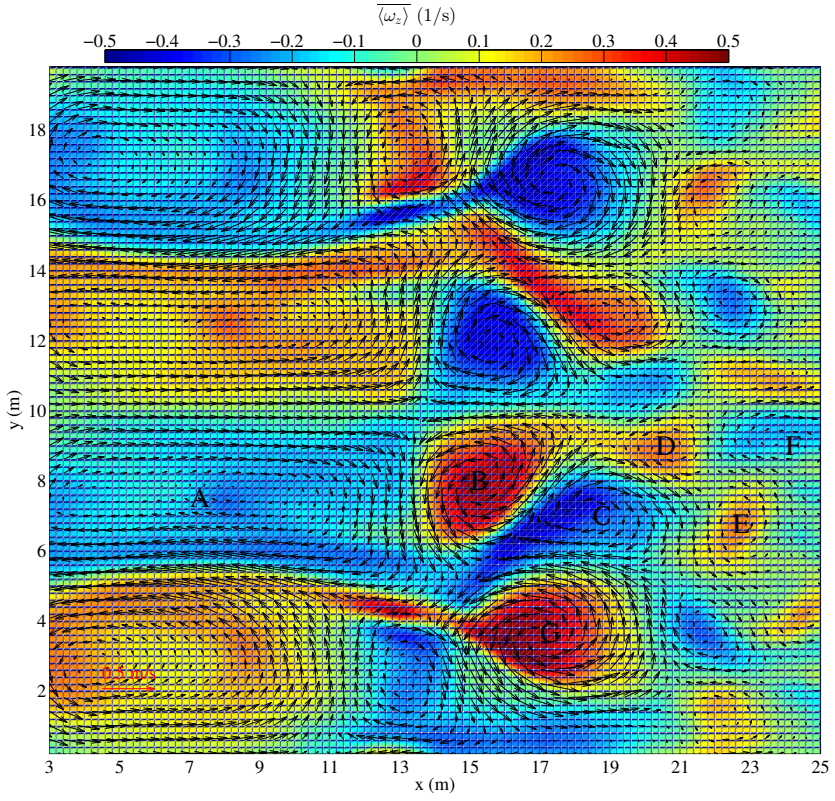

(b) H = 0.3 m

Figure 7: The distribution of the time- and depth-averaged vertical vorticity field overlain by the time- and depth-averaged current field over 10 wave periods ($40T - 50T$)**. (a)** H **= 0.2 m, and (b)** H **= 0.3 m (Wei et al. (2017)). Note that different vector and color scales are used in the two plots. The alphabet letters indicate the circulation cells cross the wave basin.**

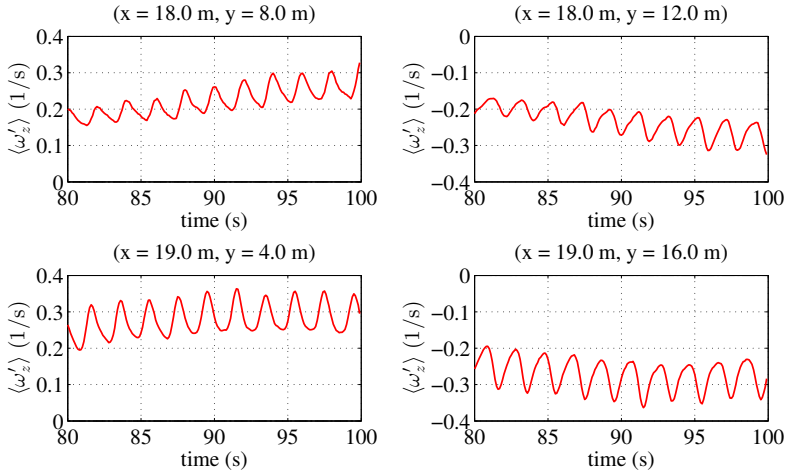

Figure 8: The time-series depth-averaged vertical vorticity generated by short-crested wave breaking with an incident wave height H = 0.2 m at four locations by using the Kelvin's circulation theorem.

Vorticity generation by short-crested wave breaking: Kelvin's circulation theorem

The circulation $\mathbf{\Gamma}$ around a closed material contour $C(t)$ is defined by

$$\mathbf{\Gamma}(t) = \oint_C \vec{u} \cdot \mathrm{d}\vec{s} = \iint_{\vec{S}} \vec{\omega} \cdot \mathrm{d}\vec{S} \tag{13}$$

where $\vec{u}$ is the velocity vector; $d\vec{s}$ is an element along the closed contour C; $\vec{\omega}$ is the vorticity; $\vec{S}$ is a surface vector bounded by the contour boundary C, and its direction is normal to the surface of the boundary. The depth-averaged vertical vorticity $\langle\omega_z'\rangle$ (a superscript prime sign is added to differentiate the vorticity defined in Eq. (12)) is obtained by

$$\langle\omega_z'\rangle = \frac{1}{S}\left(\langle u_x\rangle s_x + \langle u_y\rangle s_y\right) \tag{14}$$

where $(\langle u_x\rangle, \langle u_y\rangle)$ is the depth-averaged horizontal velocities, (s_x, s_y) is the element unit vector along the contour, and S is the surface area of the contour. Wei et al. (2017) pointed out that the vertical vorticity $\langle\omega_z'\rangle$ in Eq. (14) is a macroscopic measure of horizontal rotation of flows, as it is influenced by the configuration of the contour. After obtaining a time series of the vertical vorticity profile, the vorticity generated by wave breaking can be estimated by

$$\Delta\langle\omega_z'\rangle = \langle\omega_z'\rangle(t_0 + \Delta t) - \langle\omega_z'\rangle(t_0) \tag{15}$$

where t_0 is the moment when the wave crest bisects the circular array of current meters, and Δt is a certain amount of observation time afterwards. In this study, Δt is chosen to be one wave period T = 2 s.

By following Clark et al. (2012), this study also deploys a series of circular arrays of current meters in the surf zone to measure the vertical vorticity, and further estimates the amount of vertical vorticity generated by short-crested wave breaking. The diameter of individual current meter circle is 1 m, and there are 100 current meters equally spaced along the circle. The total duration for measurement is also 10 waves from 80 s to 100 s. Wei et al. (2017) showed that for the case with H = 0.3 m the distribution of time- and depth-averaged vertical vorticity measured by current meters based on Eq. (15) is similar to the simulated time- and depth-averaged vertical vorticity by GPUSPH as shown in Figure 7(b). Figure 8 shows the measured time-series vertical vorticity by following the definition in Eq. (14) for the case with H = 0.2 m. The considered four locations are along two cross-shore lines x = 18 and 19 m, where the short-crested waves break. For each cross-shore line, the two alongshore locations are symmetric with respect to y = 10 m. As a result, the magnitudes of 10 waves averaged vertical vorticity at the two locations are very similar, but with an opposite sign. Furthermore, the measured vorticity is also periodic over time, and the period is equal to the incident wave period T = 2 s. Overall, this study confirms the finding of Peregrine (1998) that short-crested wave breaking generates vertical vorticity and drives horizontal flow rotations in the nearshore zone.

CONCLUSIONS

In this paper, we followed our previous work in Wei et al. (2017) and conducted extra numerical experiments to investigate short-crested waves in the surf zone by using the SPH model, GPUSPH. The waves were generated by using the intersecting wave trains method of Dalrymple (1975). Then we validated the model for simulating short-crested waves by a set of laboratory experiment involving oblique wave incidence near the beach. The major work of this study was to analyze the breaking wave profile, the current field, and the vertical vorticity field under short-crested wave breaking over a planar beach by comparing two incident wave heights H = 0.2 m and 0.3 m. Key contributions and findings in this study include: (1) Short-crested waves generated by a smaller incident wave height break over the upper planar beach, resulting in a weaker rip current field and a different nearshore circulation pattern when comparing with a higher incident wave in Wei et al. (2017). The non-uniformity of short-crested wave breaking alongshore drives 3D vortex structures and multiple nearshore circulation cells. (2) This study further confirms that breaking of short-crested waves generates vertical vorticity, which describes the horizontal rotation of flows. Rip currents are generated in a region with opposite signed vertical vorticity.

ACKNOWLEDGEMENTS

The authors acknowledge the support from the Office of Naval Research, Littoral Geosciences, and Optics Program. The authors also acknowledge the ATHOS Consortium and its member organizations for their contributions to the GPUSPH code (`http://www.gpusph.org/`). The numerical simulations were carried out at the Maryland Advanced Research Computing Center.

References

D. B. Clark, S. Elgar, and B. Raubenheimer. Vorticity generation by short-crested wave breaking. *Geophysical Research Letters*, 39(24), 2012.

R. A. Dalrymple. A mechanism for rip current generation on an open coast. *Journal of Geophysical Research*, 80(24):3485–3487, 1975.

R. G. Dean and R. A. Dalrymple. Water wave mechanics for scientists and engineers. *World Scientific, Advanced Series on Ocean Engineering*, 2, 1991.

J. Hammack, N. Scheffner, and H. Segur. Two-dimensional periodic waves in shallow water. *Journal of Fluid Mechanics*, 209:567–589, 1989.

J. Hammack, N. Scheffner, and H. Segur. A note on the generation and narrowness of periodic rip currents. *Journal of Geophysical Research: Oceans*, 96(C3):4909–4914, 1991.

A. Hérault, G. Bilotta, and R. A. Dalrymple. SPH on GPU with CUDA. *Journal of Hydraulic Research*, 48 (S1):74–79, 2010.

D. Johnson and C. Pattiaratchi. Boussinesq modelling of transient rip currents. *Coastal Engineering*, 53 (5):419–439, 2006.

D. H. Peregrine. Surf zone currents. *Theoretical and Computational Fluid Dynamics*, 10(1-4):295–309, 1998.

Z. Wei and R. A. Dalrymple. Numerical study on mitigating tsunami force on bridges by an SPH model. *Journal of Ocean Engineering and Marine Energy*, 2(3):365–380, 2016.

Z. Wei, R. A. Dalrymple, A. Hérault, G. Bilotta, E. Rustico, and H. Yeh. SPH modeling of dynamic impact of tsunami bore on bridge piers. *Coastal Engineering*, 104:26–42, 2015.

Z. Wei, R. A. Dalrymple, E. Rustico, A. Hérault, and G. Bilotta. Simulation of nearshore tsunami breaking by Smoothed Particle Hydrodynamics method. *Journal of Waterway, Port, Coastal, and Ocean Engineering*, 142(4):05016001, 2016.

Z. Wei, R. A. Dalrymple, M. Xu, R. Garnier, and M. Derakhti. Short-crested waves in the surf zone. *Journal of Geophysical Research: Oceans*, 2017.